Study of Contrast-to-Noise Ratio performance of Tungsten/Silver and Tungsten/Rhodium source/filter configuration for low dose mammography applications

David Jurado Romero*
Universidad de los Andes, Bogotá, Colombia.
(Dated: June 3, 2022)

Detection of early breast cancer signs and lesions such as malignant microcalcifications is crucial for early diagnosis and treatment. X-ray mammography has been the leading technique to achieve early detection throughout the years and mammogram systems have improved in providing better quality image while reducing total radiation dose to the patient. It is known that image quality relies heavily on the X-ray spectrum configuration used, which is mainly defined by the use of a polychromatic source with a defined anode material and the use of a filtering material. This study compares anode/filter image quality through Contrast to Noise Ratio measurements of different images obtained by the use of Tungsten/Silver and Tungsten/Rhodium anode/filter configurations under the same distance, energy and time exposure conditions. The comparison between both configurations show that for the total dose fraction of each configuration, silver provides a better Contrast-to-Noise Ratio performance on benign and malignant microcalcifications. However, it is also shown that the total dose emitted to the sample is also significantly higher. Which is a major drawback on medical systems.

I. INTRODUCTION

Breast cancer is the leading cause of cancer diagnosis in women, and it is also the main cause of death by cancer in the world [10, 24]. It is also estimated that more than 30% of newly diagnosed cancer cases amongst women will be related to breast cancer [8]. Early diagnosis and detection of breast cancer is crucial to improve quality of life and survival rates by aiming to find early signals on preclinical stage, whilst also reducing any residual and invasive practices which might represent a risk factor for future medical complications [9].

There is evidence that suggest the association of morphological appearance of breast microcalcifications and breast cancer, which suggests microcalcifications as an important early sign of cancer prognosis [1, 21]. There are two types of breast microcalcifications that have been characterized on a molecular level; type I composed of calcium oxalate dihydrate also known as Weddellite ($CaC_2O_4 \cdot 2H_2O$) and type II composed of hydroxyapatite ($Ca_5(PO_4)3(OH)$), type II μCs are mostly related with subsequent cancer development whilst type I are mostly related with benign lessions [23].

The most common and important diagnosis method via imaging is X-ray mammography, which is applied worldwide and has become the standard technique for diagnosis in the last two decades [16]. The combination of a molybdenum anode and molybdenum filter (Mo/Mo) has been considered the optimal choice for mammographic X-ray tubes for years, and most of the commercial systems in clinical use have this anoode/filter configuration. However, different combinations of anode/filter have been studied throughout the years such as Rh/Rh and W/Rh. This last one has proven a reduction on gladular dose to breast tissue of about 50% compared to conventional Molybdenum systems without significant reduction in contrast [2].

However, several authors [5, 12] have studied and investigated the different factors that affect choice of X-ray spectra and how much dose is required to achieve a certain contrast-to-noise ratio. It has been shown several times [7, 15] the important role of characteristic energies of anode material and how it affects the optimum photon energies to achieve a certain signal-to-noise ratio whilst minimizing the deposited dose. Conventional low dose mammography energies range from 20keV to 34keV. On the other hand, Mo characteristic X-rays are found at 17.4 keV ($k\alpha$) and 19.8 keV ($k\beta$) [4]. Other anode materials such as silver (Ag) might seem optimal for low dose mammography imaging applications since Ag characteristic X-rays are found in nearby energies that are in between the conventional operation range for low dose mammography at 22.6 keV ($k\alpha$) and 24.6 keV ($k\beta$) [**?**]. Similarly, the use of Ag filters could also be translated on an increase of contrast-to-noise ratio values for different anode materials. Literature that refers to the study of Ag as material for medical applications on X-ray imaging is sparse, which is a motivation on characterizing its role in Anode/filter configurations.

* Institutional Email: gd.jurado10@uniandes.edu.co

II. THEORETICAL FRAMEWORK

A. Contrast in X-ray imaging

Contrast in X-ray imaging works under the principles of the Beer-Lambert law. Contrast distinction of two optical paths are necessarily related to the attenuation coefficient since this value represents the probability of a photon to be absorbed by a material. Given two materials where an object with attenuation coefficient μ_2 with a defined geometry is immersed in a medium with attenuation coefficient μ_1.

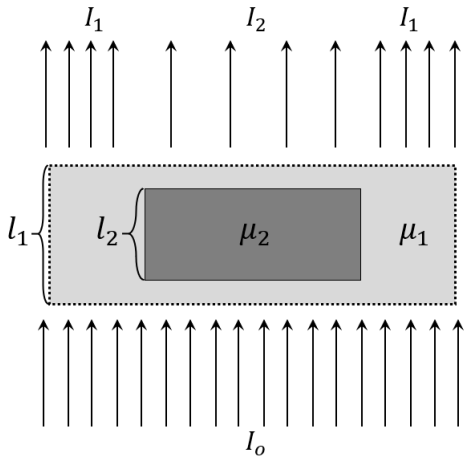

Figure 1. Diagram of the optical flux described by photons trespassing an object with two different attenuation coefficients. $\mu_1 \neq \mu_2$

Since μ_1, μ_2 give us the probability of absorbtion per lenght unit, the probabilty of a photon being detected after it trespasses the sample is given by $\mu \cdot l$. The total intensity the detector will recieve on each region is given by the values I_1 and I_2. Which are related to the Beer-Lambert principle as

$$I_d = I_o e^{(-\mu l)} \tag{1}$$

Using the contrast definition as the weighted difference of intensities [**?**]:

$$C = \frac{|I_1 - I_2|}{I_1} \tag{2}$$

And each optical path under Beer-Lambert law

$$\begin{aligned} I_1 =& I_o \exp(-\mu_1 l_1) \\ I_2 =& I_o \exp[-\mu_2 l_2] \exp[\mu_1 (l_2 - l_1)] \\ I_2 =& I_o \exp[l_2(\mu_1 - \mu_2) - \mu_1 l_1] \end{aligned}$$

The contrast then is given by a function of the difference between the attenuation coefficients and the immersed object width l_2

$$C = 1 - I_o \exp[l_2(|\mu_1 - \mu_2|)] \tag{3}$$

On the other hand, for a polychromatic energy source $I_o(\lambda)$, and a non-ideal detector plane. The two dimensional projection of the contrast is given by [**?**].

$$C(x,y) = 1 - \int I_o(x,y,\lambda) e^{-(\mu_1(\lambda)-\mu_2(\lambda))T_o(x,y)} D(\lambda) d\lambda \tag{4}$$

Where $T_o(x,y)$ is the projected geometry of the object on the detector and $D(\lambda)$ is the detector response to a photon with energy λ. This case is mostly relevant on medical applications, since most of the X-ray sources are polychromatic [**?**]. The attenuation coefficient of each material is crucial for the characterization of samples and microcalcification classification. For type I (Weddellite) and type II (Hydroxyapatite), the attenuation coefficient under different energy values is given by Figure 2 [19].

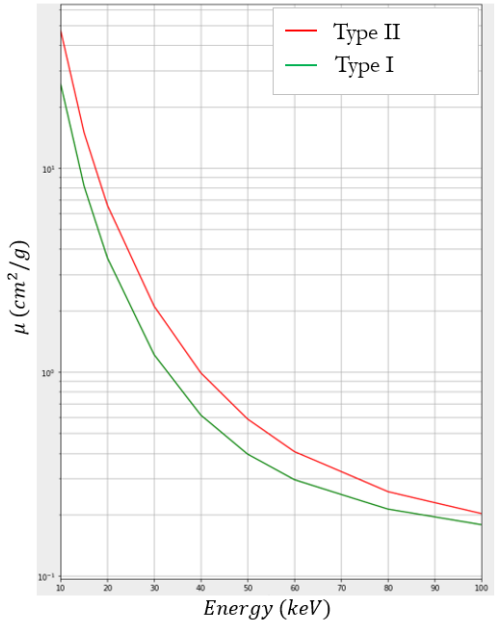

Figure 2. Absorbtion coefficient μ in relation to different energy values from 10 keV to 0.1MeV, difference between both attenuation coefficients is greater at lower energies, Hydroxyapatite (Type II μCs) is brighter on a mammography than Weddellite (Type I μCs)[18]

B. Light-matter interactions

When photons cross a section with matter, depending on the energy regimes relevant to medical applications, said photons can interact with the atom configuration

of the material. At high energy regimes, such interaction is mostly given by pair production. However, this requires $h\nu > 1MeV$ which are energies outside the focus of medical applications. Conversely, photoelectric effect, Compton effect and Rayleigh scattering are the interactions that contribute the most to the attenuation coefficient of each material inside the medical application energy range [18].

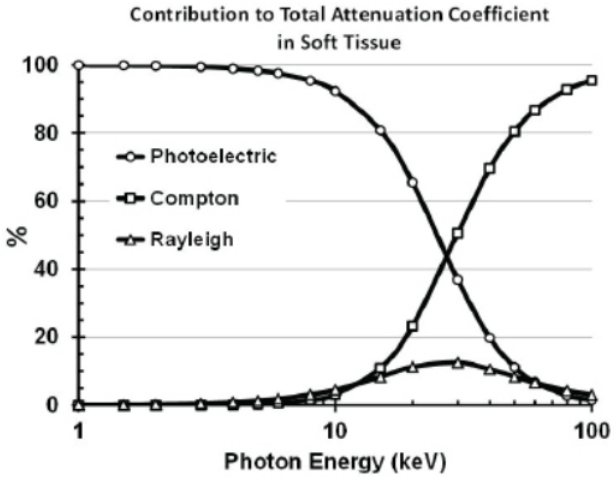

Figure 3. Light-matter phenomena that contributes to the total attenuation coefficient value in soft tissue, low dose mammography energy ranges between 20keV and 34keV, where Compton and photoelectric interactions are most common [22].

C. X-ray image evaluation. Contrast to noise ratio

Contrast to noise ratio (CNR) is an statistical measurement used to asses image quality when a detector is recieving a background and an object signal, it compares both distributions of information by computing [3].

$$CNR = \frac{|S_O - S_B|}{\sigma_B} \tag{5}$$

Where

$$S_O = \frac{1}{N_o} \sum_{j,k \in S_O} (s_j, s_k) \quad S_B = \frac{1}{N_b} \sum_{j,k \in S_B} (s_j, s_k), \tag{6}$$

The mean signal of the object and background noise and σ_B is the standard deviation of the background, which is a measure of background noise. To achieve this measure, it is necessary to choose a region of interest (ROI). In this case, this ROI represents a region with a type I or type II calcification.

III. EXPERIMENTAL FRAMEWORK

To evaluate and characterize the performance of Ag as a filter on a mammography system, it is necessary to use an experimental x ray imaging setup that mimics a clinical mammography setup. This is done in the High energy physics laboratory using the X-ray detection setup shown in figure 4. It consists of a polychromatic continuous X-ray source with a 10-100keV energy range with a focal spot of 5μm. The anode of this X-ray source is a W anode with a tube current that can reach 200μA.

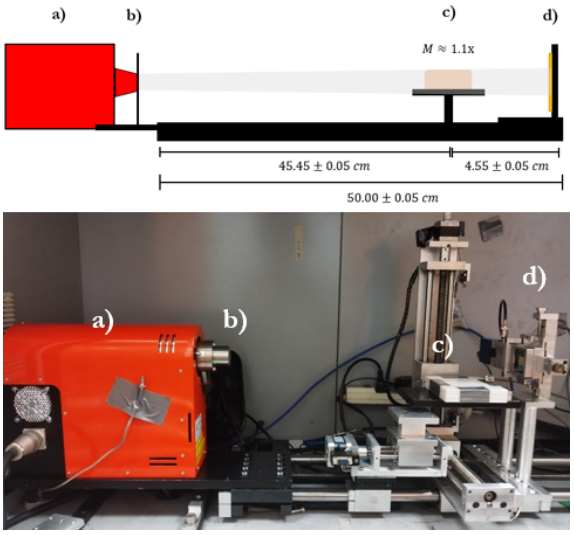

Figure 4. Experimental setup used in the high energy physics laboratory at Uniandes for x ray imaging using an Ag filter. a) Polychromatic X-ray Source with a Tungsten anode at 30kV. b) 0.025mm width Ag filter, c) UAP phantom with two μCs planes. d) Semiconductor detector Medipix3RX CdTe.

For each image, it is necessary to execute two series of data collection. Flat field and sample collection. Flat field imaging is done by removing the sample from the setup, this gives us information about the spectrum, detector and kerma of the laboratory which then is used to make a flat field correction. Every flat field data collection was made by taking 600 images with a time exposure integral of 5s. The final flat field image corresponds to the sum of the 600 images. The total flatfield measure time is 50 minutes with the main purpose of ignoring statistical effects of the source and detector. Flat field correction is necessary to cancel image artifacts that are caused by distortions in the x ray path and to reduce systematic error effects.
After flat field measurements are done, a series of images are taken with the sample, these series correspond to 120 images with a time exposure integral of 5 sec-

onds. The sample used is a PMMA phantom with two planes of Type I and type II μCs with 300 μm and 600 μm diameter as shown in the figure 7.

A. X-ray source

The X-ray source used for this experiment is the Hamamatsu L6602 that makes use of a Tungsten (W) anode and a Berilium window. This source has to undergo a pre-heating process, which requires the user to ramp up the current and voltage of the source until it reaches its maximum value throughout a certain time gap. This source has a collimator that redirects photons through a quasiplanar trajectory as shown in the figure 5. Source conditions were low dose mamography energy and dose conditions, which corresponds to a source voltage of 30keV with a 50uA current. These photons

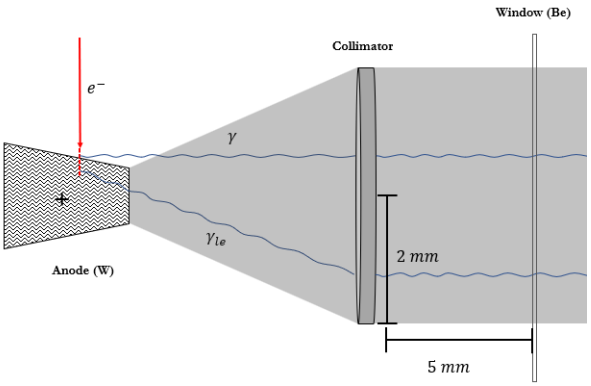

Figure 5. Optical path of photons that are reemited from the anode after being produced under anode excitation. The electrons accelerated by the source potential strike the anode and the energy released via interaction with the anode atoms produces X-ray photons. These photons may have an uneven distribution due to heel effect [a] like on the trajectory γ_{le}. These photons are then collimated. Narrowing the beam of particles and redirecting the photom trajectories, fixing the aperture angle. Finally, the collimated angle trespasses a Berylium window which has a minimal X-ray absorption coefficient.

[a] Heel effect is an X-ray imaging artifact that is produced by the early absorption of a photon due to differences in the optical path, where if one photon trespasses more anode material it might, on average, be absorbed earlier, giving an uneven distribution on the detector, flat field correction can be used to reduce heel effects on imaging.

finally go through a Beryllium window that is almost invisible through X-rays, the collimator angle aperture is negligible for the distances used in this experiment but might be important to consider in different setups.

B. Filter

The filter is one of the most important parts of this setup, its role is to modify the X-ray spectrum radiated to the sample. For this experiment, we used three different spectra that correspond to three different use of filters; raw imaging without filter, 25μm silver filtering and 50μm Rhodium filtering. The spectra of each case can be simmulated using the TASMICS simmulation tool for Tungsten anode, this can be seen at figure 6.

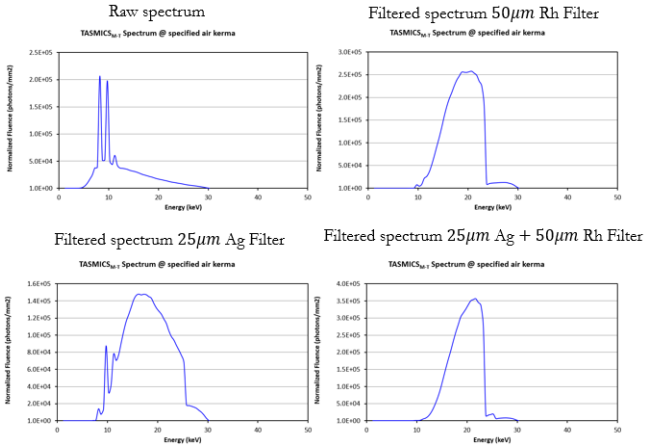

Figure 6. TASMICS [a] simulation using same source conditions which include 30keV source voltage and 5uA current. It is also assumed the specific air kerma has a value of 1 mGy []. First image corresponds to the raw spectrum of the source. As expected, $K\alpha$ and $K\beta$ lines are visible and correspond to the characteristic energies for W. The second image corresponds to the filtered spectrum using a 50μm Rhodium thin plate, the average energy has a value of 18.8 keV and the effective energy 17.1 keV. This might represent an average low radiation dose on the patient as literature specifies of the W/Rh setup []. On the other hand we have the Ag filtered spectrum using a 25μm Ag thin foil. In this case, $K\beta$ is still visible on the spectrum but the average energy is displaced to 17.4 keV. At the same time the new effective energy has a value of 14.7 keV. Finally, we have a combination of the two filters but as expected, the effect is similar as only having a Rh filter due to Rh having a higher density it already filters the same energy ranges as Ag.

[a] Tables can be found on the appendix

C. Phantom

To achieve the evaluation of X-ray imaging methods, it is necessary to have *in situ* samples that permit high radiation exposure without changing its initial conditions or degrading the quality of the sample, this can be done with biological samples and with materials that simulate the attenuation coefficient of biological tissues

under X-ray absorption (called phantoms). For this experiment, a polymethyl methacrylate (PMMA) phantom is used. PMMA has a simmilar attenuation coefficient to breast soft tissue [17] and it is easily available. Inside this PMMA phantom, two microcalcification planes can be found, each plane corresponds to type I and II microcalcifications, these planes have μCs of 300 and 600 μm of diameter which will permit the evaluation of resolution and contrast for different materials and different sizes.

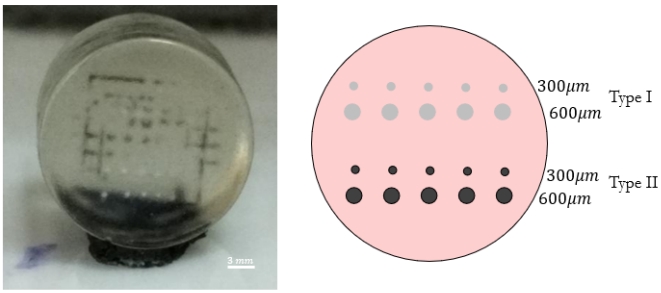

Figure 7. UAP phantom for mammography accreditation[a] with a PMMA medium of 1.2 cm thickness. Type I μCs are done with aluminium trioxide Al_2O_3 that has a similar attenuation coefficient as Weddellite.

[a] This phantom is in validation process under an article soon to be published, made by UNIANDES high energies laboratory

D. Detector

Detector plays a really important role in X-ray imaging, the detector used in this setup is the Medipix3RX, this semiconductor CdTe detector uses a photon counting detection principle that stands with a detection efficiency of 100% for energies up to 60keV. the Medipix3RX detector also has a pixel pitch of 55μm [11] which, given the semiconductor material and the low pixel size, charge sharing effects can be seen without a proper flat field correction. This detector has shown exceptional performance compared to amorphous selenium and Silica systems used in clinical setups as shown in the figure 8 [6].

IV. RESULTS

The images taken follow the procedure mentioned on the previous section, after taking each flat field [1] and

[1] Flat field and RAW individual images can be found at the appendix

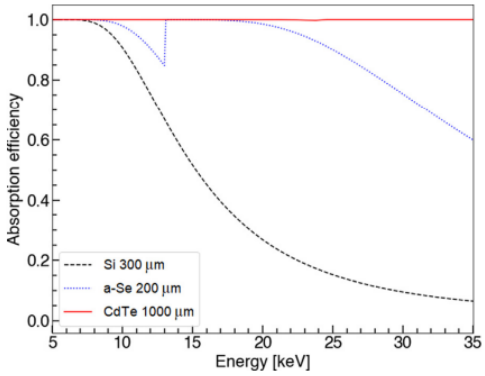

Figure 8. Absorption efficiency as function of incident X-ray photon energies for different sensor materials. Taken from [6].

raw sample images, a flat field correction is done, this flat field correction follows [20].

$$[I]_c = \frac{[I]_{RAW}}{[I]_{FF}} \tag{7}$$

Raw images also require correcting dead pixel artifacts, to solve dead pixel artifacts, a cubic interpolation is used such that every pixel with no counts has an interpolated value. The interpolation parameters are given by other pixels intensities. Pre-processed images with these two procedures are shown in figure 9 . ROI selection is achieved automatically, aided by a detection

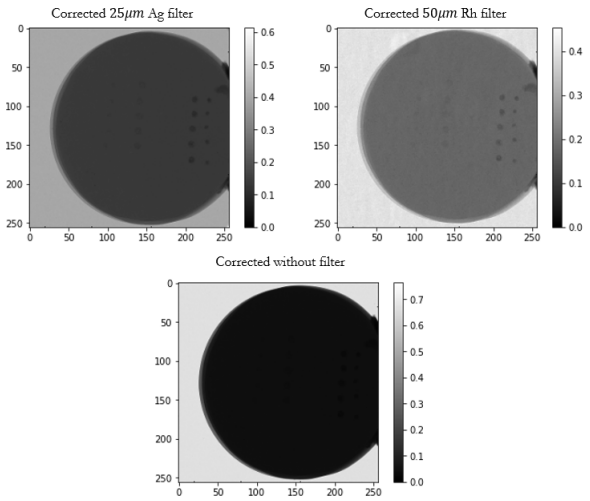

Figure 9. Pre-processed images that correspond to each case studied, Ag, Rh and no filter, this pre-process includes flat field correction which explains the color bar scale and dead pixel interpolation so no values diverge during flat field correction.

algorithm developed to characterize μCs at low contrast conditions [13]. After ROI is chosen for each μCs, an spherical mask is used to classify background signal and calcification signal using the procedure showed at figure 10.

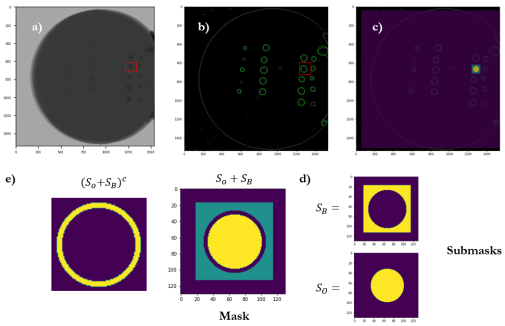

Figure 10. Selection process for ROI and mask creation. a) Pre-processed image with flat field correction, red square represents the section that will be selected by the algorithm. b) algorithm detection visualization. c) Mask automatically generated by the algorithm. Knowing the centre and the radius of each μC, the algorithm can then identify the region inside and outside the object detected, in this way, both the background and the μC can be on a separate signal as shown at d). both submasks represent the separate signals to measure CNR. e) To ignore border effects, the region immediately outside the μC is ignored. In this case, the algorithm used a 600μ m Type II μC.

V. DISCUSSION

CNR as a tool to assess image quality in X-ray imaging has been a common practice in imaging applications in physics. Other studies [14] have explored the relation between CNR and other parameters such as source kVp with different source/filter configurations. Ignoring dose values, W/Ag configuration seems to be statistically better for visualization purposes, achieving also high ROC scores on the automatic algorithm [13] for detection.

However, when deposited dose is taken into account, the radiation dose received while using a silver filter is a whole order of magnitude higher than the rhodium dose as seen on the table 1. This is explained mainly by two factors. Rhodium filters more energy than Silver by being a more dense material, which is the main factor that contributes to the attenuation coefficient μ. Additionally, for this study, the Ag thin foil was half the total width of the Rh which clearly affects the total dose deposited and the CNR measure. This can be overlook if we take an equivalent fraction of dose for silver imaging, reducing the time exposure in relation to the estimated calculated dose. This follows.

$$\frac{\%ED_T(Rh)/s}{\%ED_T(Ag)/s} \approx 21\% \tag{8}$$

Putting this in perspective, a fair estimation of CNR in function of total dose would be comparing the 0.2 ED fraction of Ag filter to the total 1 ED fraction of Rh. This, of course makes Rh a way more reasonable option. Difference is given by.

$$\mathcal{C}(TED_{(\mathrm{Rh})}) - \mathcal{C}(0.2 \cdot TED_{(\mathrm{Ag})}) = 1.969 \pm 0.0077 \tag{9}$$

Where uncertainty is associated with the standard deviation of the background noise. Although for *in vivo* imaging as a non invasive method dose is an important metric to optimize, these results imply a better use in fixed biological samples where dose is not important.

Using the previously explained method, we get the CNR measures for different μCs on the phantom, including Type I and Type II μCs. We can also estimate the total dose emitted to the sample by using flat field and sample statistics for each filter, this is given in the following table.

Table I. Dose deposited over the sample, the number of events is calculated by the difference between the flat field and the raw image of each sample done over the total volume projection of the sample. The uncertainty represents detector uncertainty per event over unit of time

Filter	Number of events	time (s)	Estimated dose
None	$(3.102 \pm 0.005) \times 10^{10}\ U$	3000 s	$(1.034 \pm 0.05) \times 10^{5}\ U/s$
Ag	$(3.185 \pm 0.005) \times 10^{9}\ U$	3000 s	$(1.06 \pm 0.05) \times 10^{4}\ U/s$
Rh	$(6.661 \pm 0.005) \times 10^{8}\ U$	3000 s	$(2.22 \pm 0.05) \times 10^{3}\ U/s$

As expected, the lowest dose over time and total dose is given by the Rhodium filter, which has the highest attenuation coefficient given its density. Since each filter provides a different dose rate for the patient, it is not trivial to provide a clear relationship between CNR and dose over time. However, using the fraction of each corresponding dose rate the Estimated Dose (ED) fraction can be taken into account, the results are shown on figure 11.

VI. CONCLUSIONS

The present study focuses on a first sight analysis of X-ray spectra optimisation for medical images

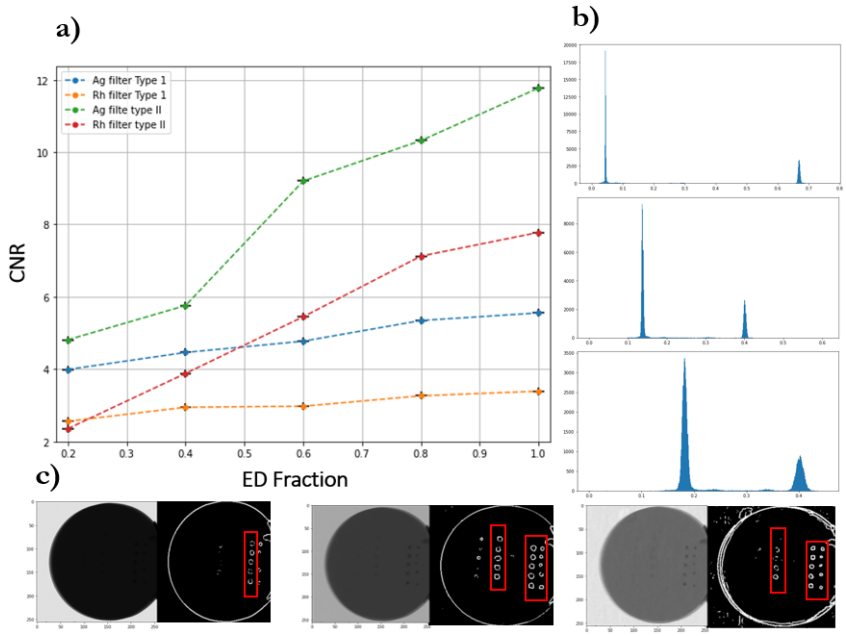

Figure 11. a) CNR relation with total dose deposited fraction, horizontal error is the uncertainty of dose rate for each material. vertical error is the standard deviation of the CNR. Type I μCs in both cases, b) Histogram representing the intensities distribution of pre-processed images, c) from left to right: images that correspond to pre-processed images with flat field corrections and regions with visible calcifications of no filter, Ag and Rh filters

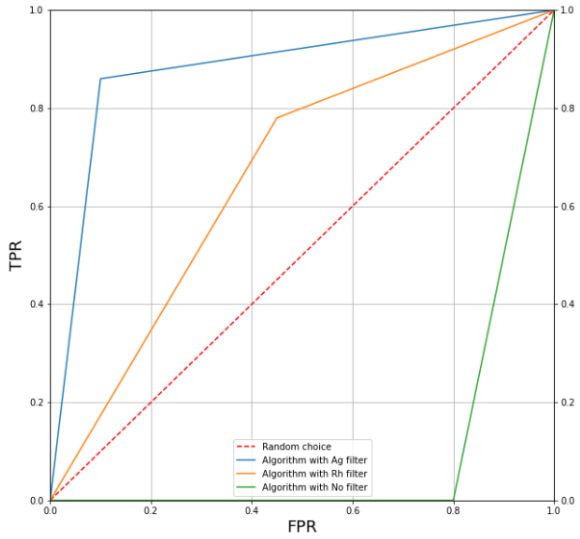

Figure 12. ROC curve for automated detection classification, note that no filter case is statistically worse than random choice. On the other hand, CNR values support the claim of the ROC curve, which is that Ag filtering works better for automated detection.

focused on breast lesions that represent early breast cancer signals, using a laboratory setup adapted to replicate imaging conditions on a conventional mammogram. This implementation allows comparative results with other optimization studies [14] and also provides a first approximation in computer vision performance around automated breast cancer detection and imaging classification. Quantitative measures of image quality like CNR are heavily related to computer vision performance, which also tells the importance on the improvement of image processing and enhancing methods that is required. By using different spectra due to the filter variation in the setup, it is possible to enhance detection capability and optimize operational lab time. However, this comes at an important dose radiation cost of almost four times the low dose W/Rh setup. This makes W/Ag not a viable option for *in vivo* medical use but a good alternative for fixed samples and other X-ray imaging aplications where dose has a minimum role.

Other studies in this topic have shown similar results [14], such as W/Rh providing a better CNR at lower dose rates. However, it is necessary to evaluate how the variation in filter width affects CNR measures directly. By simulating different setups using the TASMICS tool, it is possible to conclude that it only affects the statistics of the total spectrum (More counts are registered on the detector on a short time window). It is expected that total dose will be reduced using a 50μm Ag filter instead, and this variation will have an

exponential relation following the Beer-Lambert law.

[1] R. F. Cox and M. P. Morgan. Microcalcifications in breast cancer: Lessons from physiological mineralization. *Elsevier Review, Bone*, 53, 2004.

[2] e. a. D R DANCE. In¯uence of anode/®lter material and tube potential on contrast, signal-to-noise ratio and average absorbed dose in mammography: a monte carlo study. *The British Journal of Radiology*, 73, 2000.

[3] P. B. Denis G. Pelli. *Measuring contrast sensitivity*, volume 90. Vision research, fifth edition, 2013.

[4] D. DR. Relativistic atomic form factors and photon coherent scattering cross sections. *J Phys Chem*, 6, 1979.

[5] D. DR and D. GJ. Simulation of mammography by monte carlo calculation. the dependence of radiation dose, scatter and noise on photon energy. proceedings: patient exposure to radiation in medical x-ray diagnosis. *CEC*, 44, 1981.

[6] M. L. P.-L. L. M. Gerardo Roque, Carlos Avila and S. P. c. Study of contrast-to-noise ratio performance of a medipix3rx cdte detector for low dose mammography imaging. *Nuclear Inst. and Methods in Physics Research, A*, 2020.

[7] B. G. Gingold EL, Wu X. Contrast and dose with mo/mo, mo/rh, and rh/rh targe/filter combinations in mammography. *Radiology*, 44, 1995.

[8] N. C. Institute. Surveillance research program. *SEER*, 18, 2020.

[9] N. C. Institute. Surveillance, epidemiology, and end results. *SEER*, 2021.

[10] N. C. Institute. Seer*explorer: An interactive website for seer cancer statistics [internet]. 2022.

[11] A. Z. J Luebke, S. Procz and M. Fiederle. Suitability of the medipix2 readout-chip for radiological imaging. *Nuc Sci Symposium Conference Record, IEEE*, 2008.

[12] S. M. Jennings RJ, Eastgate RJ and E. DL. Optimal x-ray spectra for screening mmammography. *Med Phys*, 8, 1981.

[13] G. D. Jurado. Caracterización de microcalcificaciones de carcinoma mamario a partir de detecciones simuladas en fantomas con parámetros conocidos. *Tesis de grado, Uniandes*, 2021.

[14] A. A. Khaled Alkhalifah and A. Brindhaban. Image quality and radiation dose for fibrofatty breast using target/filter combinations in two digital mammography systems. *Department of Radiologic Sciences, Faculty of Allied Health Sciences, Kuwait University*, 2020.

[15] e. a. Kimme-Smith C. Mammograms obtained with rhodium vs molybdenum anodes. *AJR*, 162, 1994.

[16] J. C. L. Medina and C. Fritsch. A characterization of ultrasonic full angle spatial compounding as a possible alternative for breast cancer screening. *Acoust*, 40, 2015.

[17] C. M. M. . M. G. M. Morgan M. P. Xcom: Photon cross sections database nist standard reference database 8 (xgam). *National Institute of Standards and Technology*, 1, 2010.

[18] E. National Academies of Sciences and Medicine. *Airport Passenger Screening Using Backscatter X-Ray Machines*. 2015.

[19] E. B. Podgorsak. *Radiation Physics for Medical Physicists*, volume 1. Springer-Verlag Berlin Heidelberg, second edition, 2010.

[20] T. Pradhan and A. Khare. Feynman diagram method for atomic collisions. *Institute of Physics, Bhubaneswa*, 1975.

[21] L. R. Diagnosis of tumors of the breast by simple roentgenography; calcifications in carcinomas. *Am J Roentgenol Radium Ther*, 65, 1951.

[22] R. N. Squire. *Fundamentals of Radiology*. Harvard University Press, fifth edition, 1997.

[23] D. S. Tabar L, Tony Chen HH and S. RA. Mammographic tumor features can predict long-term outcomes reliably in women with 1-14-mm invasive breast carcinoma. *Cancer*, 101, 2004.

[24] W. E. Wild CP and S. BW. World cancer report: Cancer research for cancer prevention. *International Agency for Research on Cancer*, 586, 2020.

VII. APPENDIX

For code, resources and data, refer to `https://github.com/DavidJHub/ProyectoLabAv`

Aprobado: _____

Carlos Ávila, Ph.D.